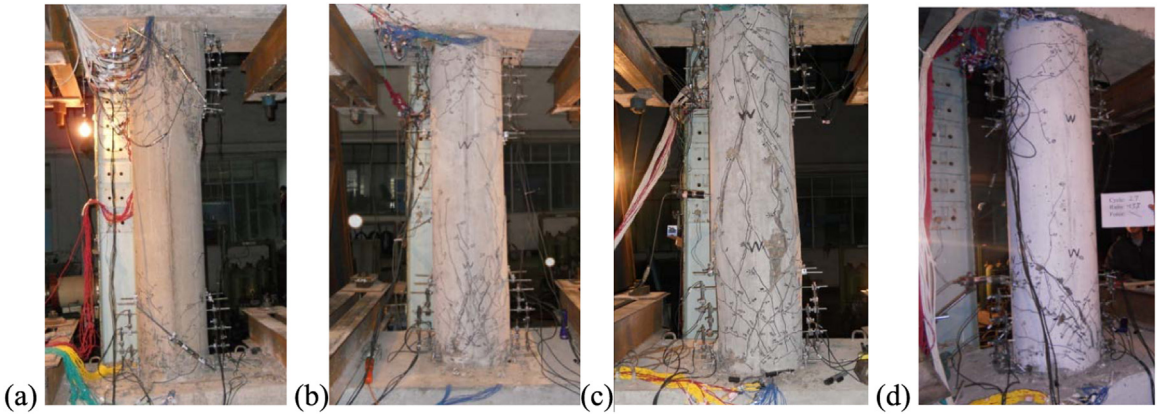

Fig. 5. Failure modes at the end of the tests.

δ = 2.0% because of concrete crushing at the top plastic hinge of the column.

In specimen C-2, symmetric flexural cracks occurred at both ends of the specimen at δ = 0.5%. At δ = 0.75%, diagonal cracks occurred, and hoop bars yielded earlier than C-1. The longitudinal bars yielded at δ = 1%, and the yield load-carrying capacity P_y reached 271 kN and − 284 kN (see Fig. 4(b)). After the peak strength P_u = 312 kN at δ = 1.25% and − 321 kN at δ = −1.0%, bond-slip cracks along the longitudinal bars occurred in the range of 500 mm at the bottom end, and spalling of cover concrete near the height of 50 mm was initiated (see Fig. 5(b)). Ultimately, C-2 failed at the second cycle of δ = 1.5% because of concrete crushing at the bottom plastic hinge of the column.

In specimen C-3, flexural cracks occurred at both tension sides of the specimen at δ = 0.3%. At δ = 0.6%, the flexural cracks were extended to diagonal cracks, and new diagonal cracks occurred at 440 mm from the bottom end. At δ = 0.8%, the diagonal cracks were occurred to the column center, and hoop bars yielded. The longitudinal bars yielded at δ = 0.9%, and the yield load-carrying capacity P_y reached 357 kN and − 435 kN (see Fig. 4(c)). After the peak strength P_u = 359 kN and − 441 kN at δ = 1.0%, target drift ratio δ was gradually reduced to δ = 0.0%, and ten load cycles re-applied at δ = 1.0%. In the load cycles, the load carrying-capacity was almost maintained. However, spalling of cover concrete initiated, and hoop strain increased continuously. At the second cycle of δ = 1.1%, the maximum crack width increased to 1.34 mm. Spalling of cover concrete occurred at δ = 1.4% (see Fig. 5(c)). Crack width in the plastic hinge exceeded 5.0 mm. The load-carrying capacity decreased to 134 kN and − 168 kN in the positive and negative loadings, respectively. Ultimately, C-3 failed at the first cycle of δ = 1.5% because of concrete crushing at the plastic hinge of the column specimen.

In specimen C-4, flexural cracks were initiated at P = 180 kN corresponding to δ = 0.2%, and diagonal cracks occurred at δ = 0.5%. The longitudinal bars and hoop bars yielded at 0.8%, and the yield load-carrying capacity P_y reached 299 kN and − 341 kN (see Fig. 4(d)). After the peak strength P_u = 302 kN and − 351 kN at δ = 1.0%, the load-carrying capacity decreased due to the ten times repeated cyclic loadings at δ = 1.0%. At δ = 1.1%, bond-slip cracks along the longitudinal bars occurred at the top and bottom end. At δ = 1.4%, diagonal cracks expanded to the column center (see Fig. 5(d)). Ultimately, C-4 failed at the first cycle of δ = 1.5% due to shear failure.

In specimen C-1, flexural failure is governed due to large shear span ratio 2.57. On the other hand, specimens C-2 to C-4 with relatively lower shear span ratio 2.16 exhibited shear failure. The number of the flexural cracks was increased in specimen C-1, while the number of the diagonal cracks was increased in specimens C-2 to C-4.

3.2. Deformation Capacity

Table 2 lists the ultimate drift ratios δ_u and ductility ratio μ of column specimens. C-1 showing flexural failure due to large shear span ratio 2.57 exhibited the greatest deformation capacity δ = 2.0% and ductility ratio μ = 2.68 (average value). On the other hand, C-3 showing shear failure due to lower shear span ratio 2.16 under cyclic loading type 2 exhibited the least deformation capacity (δ = 1.2%) and ductility ratio μ = 2.19. This is because 1) low shear span ratio 2.16 increased the shear demand that increases the diagonal cracks and concrete damages in the specimen (see Figs. 5(c)); and 2) critical diagonal cracks were initiated at the first load cycle, which indicates the column specimen was susceptible to cyclic loading type 2 describing near-fault ground motion. In C-2 under cyclic loading type 1 that describes far-field ground motion, diagonal cracks were relatively well distributed compared to those of C-3. Even though the cyclic loading type 2 was applied to C-4, premature shear failure was prevented due to the reduced shear demand. As a result, the deformation capacities δ = 1.5% and ductility ratios μ = 2.33 of C-2, and δ = 1.5% and μ = 2.64 of C-4 were greater than those of C-3.

3.3. Secant stiffness

Fig. 6 shows the variation of the average secant stiffness at each load cycle. The secant stiffness K_s indicates the slope between the peak positive and negative strength in the load-drift relationship.

$$K_s = \frac{|+P_i| + |-P_i|}{|+\Delta_i| + |-\Delta_i|} \quad (1)$$

where P_i = peak strength at the i^{th} load cycle, Δ_i = lateral drift corresponding to P_i.

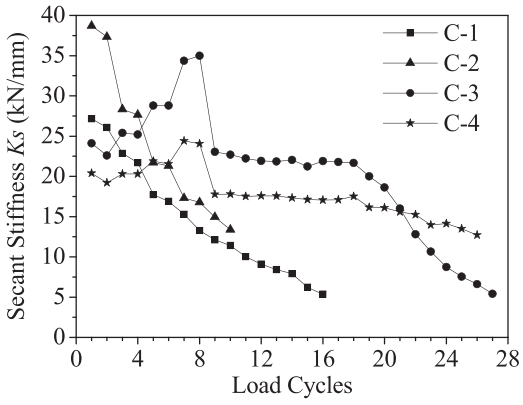

Fig. 6. Variations of secant stiffness according to load cycles.

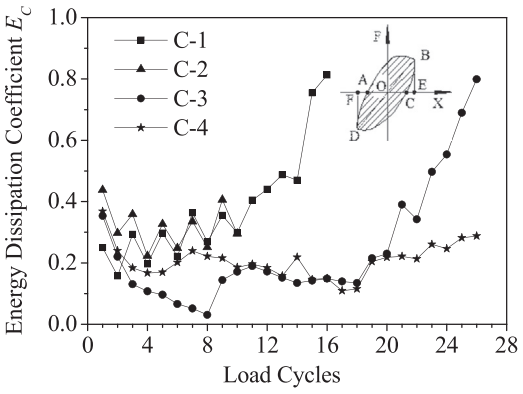

Fig. 7. Energy dissipation per load cycle.

In Fig. 6, C-2 showed greater secant stiffness K_s than that of C-1 because of greater load-carrying capacity due to shorter shear-span ratio. The secant stiffness K_s of C-1 and C-2 decreased as the load cycles increased. This is because the existing flexural-shear cracks are expanded, and a few new cracks occur as the loading amplitude increases. The secant stiffness K_s of C-1 and C-2 at $\delta = 1.5\%$ was approximately 58% and 44% of the yield stiffness K_y, respectively. On the other hand, in C-3 and C-4, the secant stiffness K_s at the 1st cycle corresponding to $\delta = 1.0\%$ was less than that of the undamaged secant stiffness K_s of C-2 at the 1st cycle. However, the secant stiffness K_s of C-3 and C-4 at the 1st cycle was almost same to that of C-2 at the 7th cycle corresponding to $\delta = 1.0\%$. From the 3rd cycle to 8th cycle, the secant stiffness K_s increased because the lateral drift ratio decreased to $\delta = 0.0\%$. After the ten times repeated load cycles at $\delta = 1.0\%$, the secant stiffness of C-3 and C-4 showed 85.9% and 85.3% of those corresponding to the 1st load cycle, respectively. The secant stiffness K_s of C-3 at the ultimate drift ratio $\delta_u = 1.2\%$ and C-4 at $\delta_u = 1.5\%$ was approximately 40% and 35% of the yield stiffness K_y, respectively.

3.4. Energy dissipation capacity

Fig. 7 shows the variation of energy dissipation capacity of the four specimens according to the number of cyclic loading. The energy dissipation coefficient E_C per load cycle was defined as follows (JGJ101-96).

$$E_C = \frac{E_D}{S_{OBE} + S_{ODF}} \tag{2}$$

where E_D = energy dissipation per load cycle defined as the area enclosed by a complete load cycle; S_{OBE} = triangular area enclosed by points O, B, and E; and S_{ODF} = triangular area enclosed by points O, D, and F.

C-1 and C-2 exhibited the similar E_C values until the 10th load cycle. In C-2 showing shear failure, however, E_C was measured until the 10th load cycle. On the other hand, after the 10th load cycle, E_C of C-1 increased due to flexural behavior. C-3 and C-4 showed lower E_C values than those of C-1 and C-2 because the cyclic loading initiated to the yield loading at the first loading step, which caused shear damage. After the 20th load cycle (i.e., $\delta = 1.1\%$), E_C of C-3 increased due to strength degradation. On the other hand, E_C of C-4 was not almost increased due to bar-slip. It should be noted that the large cyclic loading at the initial state decreased the energy dissipation capacity of the specimens.

3.5. Strain of hoops

Hoops provide confinement effect on the core concrete of a circular column, which increases the load-carrying capacity and deformation capacity. Furthermore, lateral buckling of the longitudinal bars are restrained by the hoops. Fig. 8 shows the strains of the hoops measured by strain gauges in plastic hinge of columns. According to Priestley [16], plastic hinge length l_p of a flexural member can be defined as follows.

$$l_p = 0.08l + 0.022d_b f_y \tag{3}$$

where l = column length, which was considered as a half column height H_c because the both ends of the specimen were completely fixed; d_b = diameter of the longitudinal bars; and f_y = yield strength of the longitudinal bars.

In specimen C-1 showing flexural failure, hoop strains were concentrated at the height of 150 mm and 250 mm from the bottom end of the specimen, which was almost consistent with the calculated plastic hinge length 205.5 mm. At $\delta = 2.0\%$, concrete crushing at the bottom of the specimen caused the maximum hoop strain of about 0.0025 mm/mm, which was greater than the yield strain 0.0019 mm/mm. In specimen C-2, after the hoops yielded at $\delta = 1.0\%$, hoop strain significantly increased over 0.0140 mm/mm at $\delta = 1.5\%$. As a result, large diagonal cracks and concrete crushing failure occurred. Specimens C-3 and C-4 exhibited similar hoop strain variation, except the maximum hoop strain locations at 250 mm and 150 mm from the bottom end of C-3 and C-4, respectively. After the hoops yielded at the first load cycle, crack width increased at the initial cracks. As a result, though the number of cracks of C-3 and C-4 was less than that of C-2, premature concrete damage and larger hoop strains were occurred (refer to Fig. 5).

4. Evaluation of structural performance

4.1. Load-carrying capacity

Lateral load-carrying capacities of circular columns were evaluated by Chinese design code (GB50010—2010). Compression force N was applied to the column specimens, which decreased the lateral load-carrying capacity due to the second-order effect. Thus, the nominal strength P_n was calculated as follows:

$$P_n = P_{no} - N\delta \tag{4}$$

where $P_{no} = 2M_n / H_c$; M_n = nominal flexural strength considering compression force effect. δ = lateral drift ratio of the specimens. The nominal flexural strength M_n was calculated from section analysis considering the effect of compression force N = 1210 kN (C-1), 1180 kN (C-2), 1417 kN (C-3) and 1120 kN (C-4). The lateral load-carrying capacities P_{no} of four specimens are 283 kN, 330 kN, 368 kN, and 367 kN, respectively. P_{no} and P_n of the specimens are presented as the dotted lines in Fig. 4(a) to (d). The lateral load-carrying capacities P_n decreased as the lateral drift ratio δ increased due to the second-order effect. The predictions correlated well with the tests results.

4.2. Shear strength

Shear resistance of circular columns is provided by concrete, and hoops. According to Chinese design code (GB50010—2010), the nominal shear strength V_n of the column specimen can be calculated with consideration of the contributions of concrete, transverse hoops, and applied axial load as follows:

$$V_n = \frac{1.75}{\lambda + 1} f_t b h_0 + f_{yv} \frac{A_{sv}}{s} h_0 + 0.07N \tag{5}$$

where λ is shear span ratio; f_t is tensile strength of concrete ($= 0.359 f_c'^{.55}$); b and h_0 are width and effective height of a rectangular section, respectively, which can be replaced by 1.76r and 1.6r in the circular section (r is the radius of the column section); f_{yv} is yield strength of the steel hoops; and A_{sv} is cross-sectional area of the hoops.

In test specimens, V_n in Eq. (5) were greater than the shear demand V_u by the peak strength (V_n / V_u = 316/314 = 1.01 for C-1, 318/321 = 0.99 for C-2, 360/441 = 0.82 for C-3, and 317/351 = 0.90 for C-4). Since the ratio was less than 1.0 for C-2, C-3 and C-4, shear failure

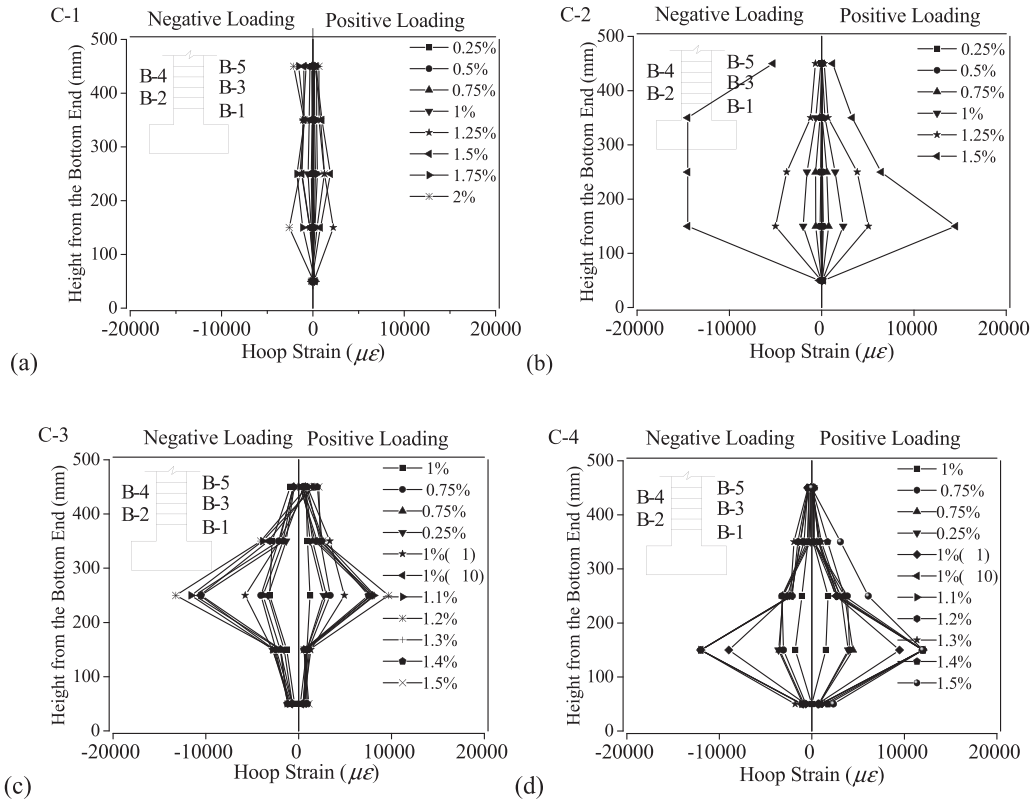

Fig. 8. Strains of hoops.

easily occurred in the test specimens.

4.3. Contributions to lateral drift

Lateral drift Δ of specimens consists of bond-slip deformation Δ_{bs}, shear deformation Δ_s, and flexural deformation Δ_f (refer to Fig. 9).

$$\Delta = \Delta_{bs} + \Delta_s + \Delta_f \tag{6}$$

Bond-slip deformation Δ_{bs} is developed by bond-slip of the longitudinal bars at the column-footing joint, which causes rotation of the column as a rigid body behavior. Fig. 10 shows the bond-slip measurement and curvature distribution in the column specimen. In the present study, uniformly distributed curvature was assumed in the measurement region.

$$\phi_1 = \frac{(\Delta_{L1} - \Delta_{R1})}{L_1 H_1} \quad \text{for region 1} \tag{7a}$$

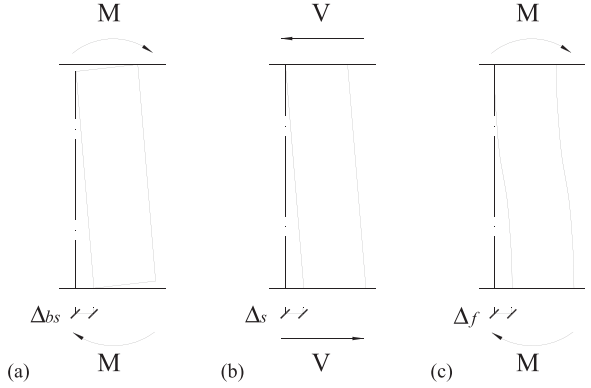

Fig. 9. Estimations of lateral drift developed by bond-slip, shear, and flexural deformations.

$$\phi_2 = \frac{(\Delta_{L2} - \Delta_{R2})}{L_2 H_2} \text{for region 2} \tag{7b}$$

where ϕ_1 and ϕ_2 = curvatures at the regions 1 and 2, respectively; Δ_{L1} and Δ_{R1} = displacements measured on left and right sides at the region 1 of the specimen, respectively; Δ_{L2} and Δ_{R2} = displacements measured on left and right sides at the region 2 of the specimen, respectively; L_1 and L_2 = horizontal distance between the linear potentiometer at the regions 1 and 2, respectively; and H_1 and H_2 = vertical distance between the linear potentiometer at the regions 1 and 2, respectively (= 30 mm and 100 mm).

Curvature ϕ_1 at the region 1 includes both the flexural curvature and bond-slip curvature. Considering the relative small length H_1 of the region 1, the bond-slip rotation θ at the bottom of the column specimen can be calculated from the curvatures ϕ_1 and ϕ_2.

$$\theta = H_1(\phi_1 - \phi_2) \tag{8}$$

The bond-slip rotation θ is simplified to be developed at the center of the curvature ϕ_1. Thus, the average bond-slip deformation Δ_{bs} is as follows.

$$\Delta_{bs} = \frac{(\theta_{top} + \theta_{bot})}{2}(H_c - H_1) \tag{9}$$

where θ_{top} and θ_{bot} = bond-slip rotation at the top and bottom ends of the specimen in Eq. (8), respectively.

As shown in Fig. 10, bond-slip deformation of C-1 increased with the increase of load cycles. After yielding of the longitudinal bars (i.e., 6th load cycle), the bond-slip deformation Δ_{bs} significantly increased under positive loading, and decreased under negative loading. In C-2, bond-slip deformation was less than those of other specimens. In C-3 and C-4, bond-slip deformation Δ_{bs} of C-4 was greater than that of C-3. This is because the specimen C-4 with larger diameter of longitudinal bars and low strength of concrete is vulnerable to bond failure.

Fig. 11 shows the shear distortion γ according to the load cycles. The shear distortion was calculated from the test measurement in the

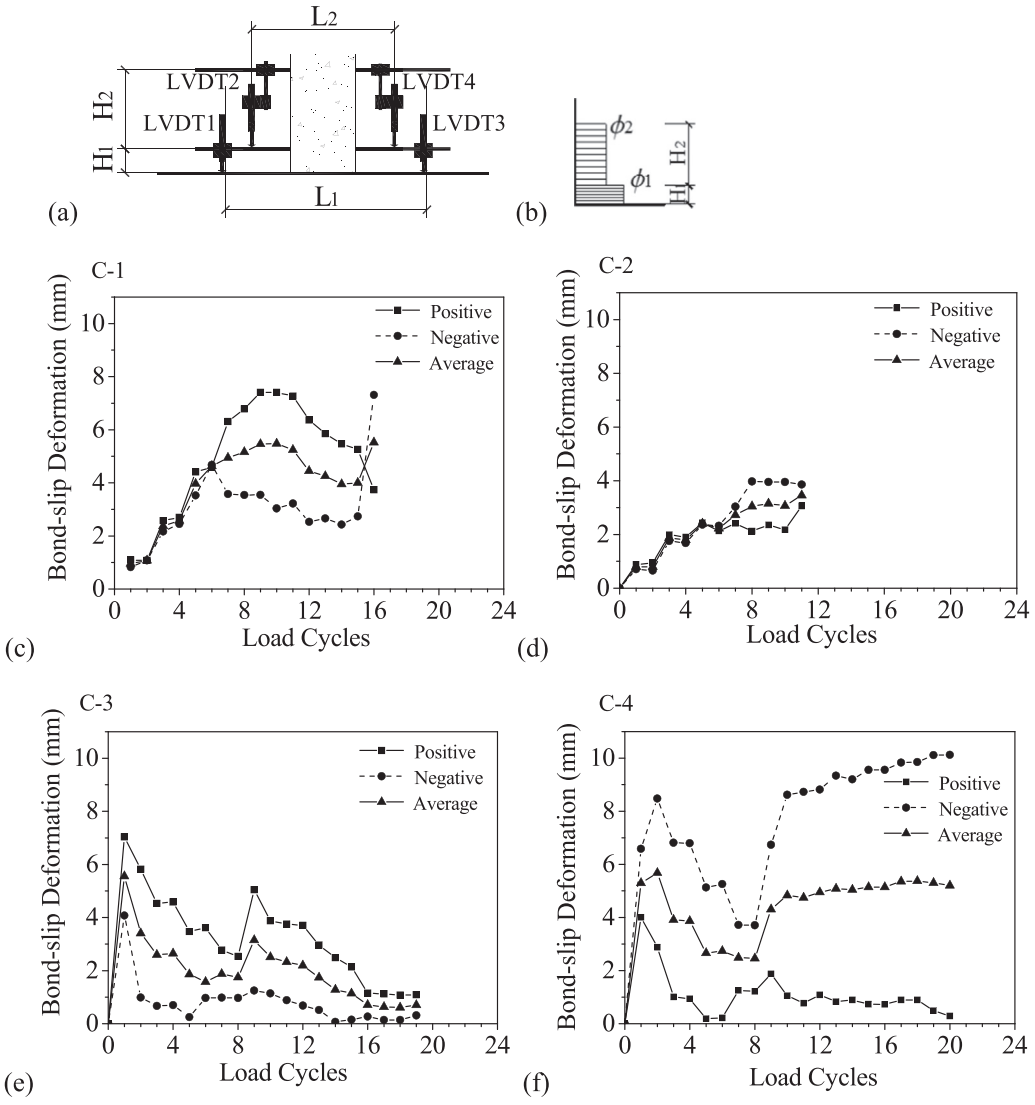

Fig. 10. Bond-slip deformation measurements.

plastic hinge region of the specimens.

$$\gamma = (\Delta - \Delta')\frac{\sqrt{a^2 + b^2}}{2ab} \tag{10}$$

where Δ and Δ' = diagonal deformations measured by the two diagonal linear potentiometers; and a and b = horizontal and vertical distance, respectively, between the ends of the diagonal linear potentiometers (= 400 mm and 400 mm).

Specimen C-1 exhibited the almost same shear distortion to that of C-2 regardless of shear span ratio. In C-3, after the initial load cycle at δ = 1.0%, the shear distortion linearly decreased due to the reduced lateral drift. In the constant ten cycles at δ = 1.0%, the shear distortion increased slightly, but the increment was only 2.3%. Ultimately, the shear distortion of C-3 under cyclic loading type 2 was greater than that

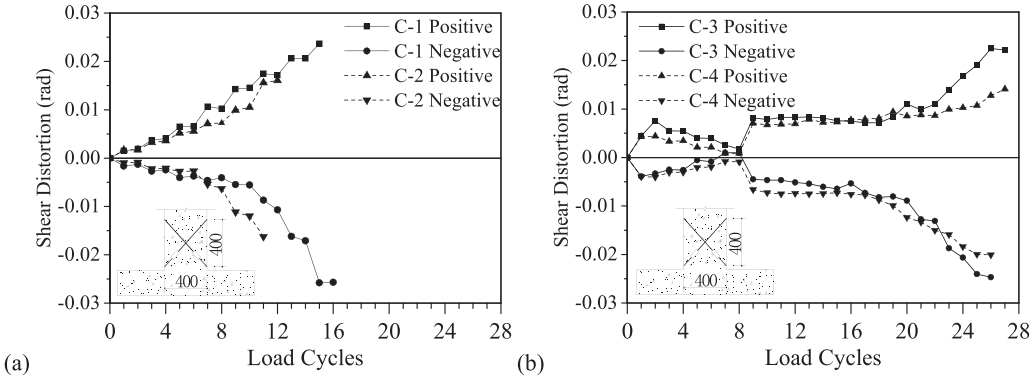

Fig. 11. Shear deformation measurements.

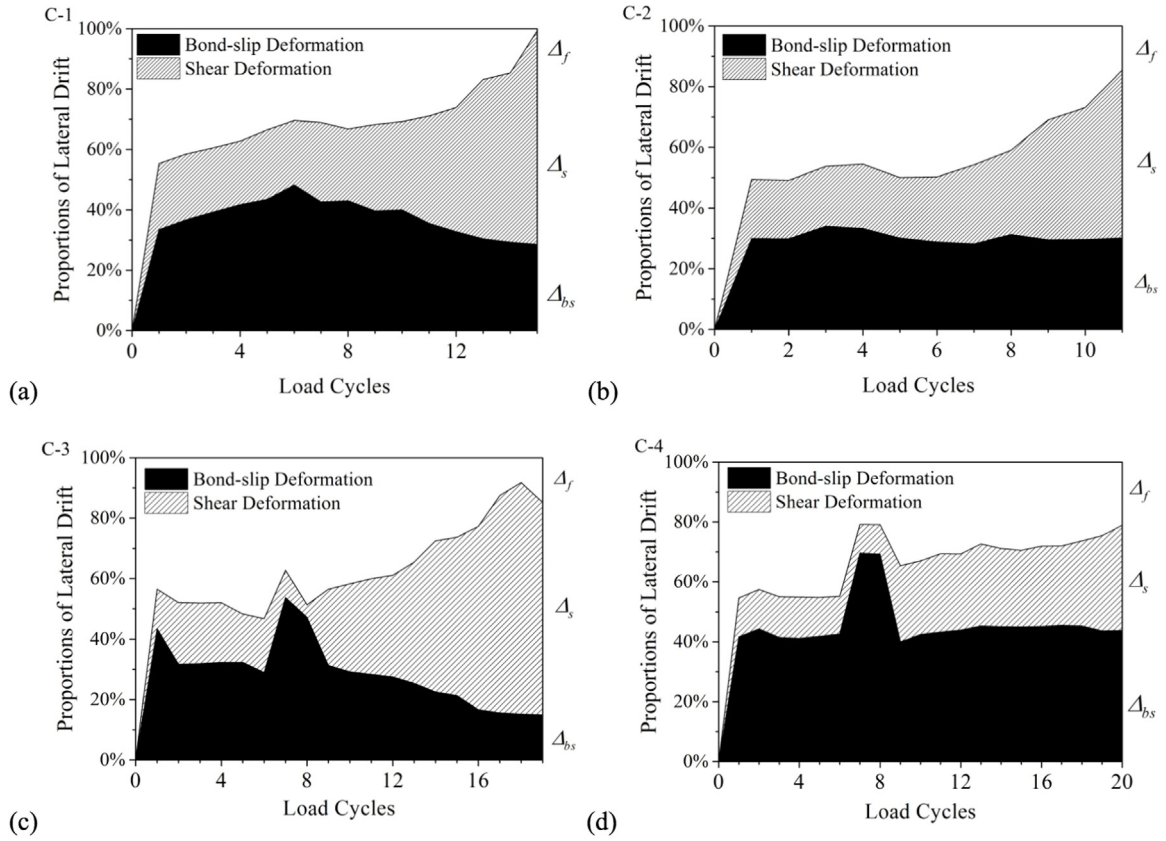

Fig. 12. Contributions of bond-slip, shear, and flexural deformations to lateral drift.

of C-2 under cyclic loading type 1.

Fig. 12 shows the ratio of each contribution of bond-slip deformation, shear deformation, and flexural deformation to the overall lateral drift measured from the test specimens. The flexural deformation was calculated by $\Delta_f = \Delta - \Delta_{bs} - \Delta_s$. The shear deformation Δ_s was calculated from the shear distortion γ. In C-1, after yielding of the longitudinal bars at the 6th load cycle, the bond-slip contribution decreased, but the shear deformation contribution increased. The contribution of the flexural deformation ranged from 2% to 45%. In C-2 with low shear-span ratio, the contribution of the flexural deformation was greater than that of C-1 because the bond-slip decreased. In C-3 with low $V_n / V_u = 0.82$, the shear deformation contribution was significantly increased due to shear failure. The contribution of the bond-slip deformation in C-4 was greater than that of C-3, which decreased the flexural deformation contribution. This result indicates that in C-4, the contribution of the bond-slip deformation was significant because of large diameter of longitudinal bars.

5. Summary and conclusions

Four RC circular column specimens with different height and reinforcements were tested under two different cyclic loadings to investigate the seismic structural performance of the RC columns. On the basis of test results, load-carrying capacity, deformation capacity, failure mode, and energy dissipation capacity of the column specimens were evaluated. The primary test results are summarized as follows.

(1) Specimen C-1 with shear-span ratio 2.56 exhibited flexural failure, which showed deformation capacity of $\delta_u = 2.0\%$. On the other hand, specimens C-2 to C-4 with shear-span ratio 2.16 exhibited shear failure, which decreased deformation capacity of $\delta_u = 1.2–1.5\%$.
(2) The lateral load-carrying capacity of the column specimens predicted by Chinese design code (GB50010—2010) correlated well with the test strengths.
(3) The number of flexural cracks in C-2 to C-4 was less than that of C-1, while the amount of diagonal cracks in C-2 to C-4 was greater than that of C-1. The number of cracks in C-3 and C-4 under the cyclic loading that describes near-fault ground motion decreased, but the damage at the initial cracks increased shear deformation and decreased energy dissipation. This result indicates that near-fault ground motion decreases the seismic structural performance of circular reinforced concrete columns with relatively small shear span ratio.
(4) The maximum hoops strain occurred between 150 mm and 250 mm of columns height, which were close to the plastic hinge length predicted by the empirical equation. The cyclic loading that describes near-fault ground motion increased the hoops strain due to strain concentration at the premature concrete damage, which increased the shear deformation.

Acknowledgement

The authors are grateful for the support provided to this research by NSFC (No. 80915002, 51208190, 51338004), National Key Research and Development Program of China (No. 2016YFC0701400, 2016YFC0701308) and Key Research and Development Program of Hunan Province (No. 2017SK2220).

References

[1] Somerville PG. Characterizing near fault ground motion for the design and evaluation of bridges. Proceedings of the Third National Conference and Workshop on Bridges and Highways; Portland, Oregon; 2002.
[2] Kalkan E, Kunnath SK. Effects of fling step and forward directivity on seismic response of buildings. Earthq Spectra 2006;22(2):367–90.
[3] Mayes RL, Shaw A, Lafayette CA. The effects of near fault ground motions on bridge

columns[C]//Workshop on the National Representation of Seismic Ground Motion for New and Existing Highway Facilities. p. 319-325; 1997.
[4] Orozco GL, Ashford SA. Effects of large velocity pulses on reinforced concrete bridge columns. Pacific Earthquake Engineering Research Center Report. Berkeley, CA, USA: University of California; 2002.
[5] Tsuno K, Park R. Prediction method for seismic damage of reinforced concrete bridge columns. Struct Eng Earthq Eng 2004;21(2):97–111.
[6] Chang SY, Li YF, Loh CH. Experimental study of seismic behaviors of as-built and carbon fiber reinforced plastics repaired reinforced concrete bridge columns. J Bridge Eng 2004;9(4):391–402.
[7] Phan V, Saiidi MS, Anderson J, Ghasemi H. Near-fault ground motion effects on reinforced concrete bridge columns. J Struct Eng 2007;133(7):982–9.
[8] Choi H, Saiidi M, Somervile P, EI-Azazy S. An experimental study of RC bridge columns subjected to near-fault ground motions. Am Concr Inst, Acids Struct J 2010;107(1):3–12.
[9] Brown A, Saiidi MS. Investigation of effect of near-fault motions on substandard bridge structures. Earthq Eng Eng Vib 2011;10(1):1–11.
[10] The People's Republic of China Industrial Standard. Building Aseismic Test Method Procedure Code (JGJ101－96).Beijing: China Building Industry Press. p. 3-13; 1997.
[11] The People's Republic of China National Standard. Technical Specification for Concrete Structures of Tall Building (JGJ3-2002).Beijing: China Building Industry Press. p. 58-67; 2002.
[12] The People's Republic of China National Standard. China Code for Designing of Concrete Structures (GB50010-2010). Beijing: China Building Industry Press; 2010.
[13] Liu Y. Experimental Research of Framework's Seismic Performance under the Near-field Earthquake [Master's Degree Thesis] 2010. Changsha: Hunan University; 2010. p. 12–47.
[14] Yi WJ, Zhou Y, Liu Y, et al. Experimental Investigation of Circular Reinforced Concrete Columns under Different Loading Histories. J Earthq Eng 2016;20(4):654–75.
[15] Park R. State-of-the-art report on ductility evaluation from laboratory and analytical testing. In: Proceedings of the 9th World Conference on Earthquake Engineering, International Association for Earthquake Engineering, Tokyo, 8; 1988. p. 605-616.
[16] Priestley MJN, Verma R, Xiao Y. Seismic shear strength of reinforced concrete columns. J Struct Eng 1994;120(8):2310–24.